Industrial Chemistry & Materials

ROYAL SOCIETY OF CHEMISTRY

PAPER

View Article Online
View Journal

Cite this: DOI: 10.1039/d5im00296f

Electron-withdrawing pyridine-functionalized g-C_3N_4-coordinated cobalt phthalocyanine for enhanced photocatalytic CO_2 reduction

Xuehua Zhang, [af] Chunlei Su,[af] Rui Shi,[b] Mingming Li, [c] Lili Fu,[d] Rongji Liu,[e] Yong Chen, *[b] Bin Li*[d] and Guangjin Zhang*[af]

To enhance the charge separation efficiency of g-C_3N_4 and facilitate electron transfer between photosensitizer and molecular catalyst, polarization and coordination strategies are used by grafting pyridine rings onto the edge of the g-C_3N_4 framework. Herein, electron-withdrawing pyridine edge-functionalized g-C_3N_4 (g-C_3N_4-P_x) was synthesized *via* facile one-step thermal polymerization of urea and 4-aminopyridine, and employed as visible-light photosensitizer hybridized with cobalt phthalocyanine (CoPc) for efficient photoreduction of CO_2. Both experimental and theoretical results confirm that electron-withdrawing pyridine grafting facilitates in-plane charge separation and directs electron migration toward the edge of g-C_3N_4, narrows its band gap for enhanced visible-light absorption, and provides dynamic coordination sites that significantly boost interfacial electron transfer from g-C_3N_4-P_x to CoPc. A significant increase in the CO yield was achieved with the optimized CoPc/g-C_3N_4-$P_{1.5}$ hybrid, reaching 14.95 mmol g^{-1} after 6 hours of visible-light irradiation—a 6.1-fold improvement over the unmodified CoPc/g-C_3N_4 (2.47 mmol g^{-1}). This work provides a facile approach for developing highly efficient hybrid photocatalysts for CO_2 reduction and improving the charge separation and visible-light absorption in organic semiconductors.

Keywords: CO_2 photoreduction; Cobalt phthalocyanine/g-C_3N_4 hybrid photocatalysts; Polarization engineering; Directional electron transfer; Coordination interaction; Electron-withdrawing effect.

Received 16th October 2025,
Accepted 11th December 2025

DOI: 10.1039/d5im00296f

rsc.li/icm

1 Introduction

Photocatalytic carbon dioxide (CO_2) reduction using solar energy represents an ideal approach to address energy and environmental challenges, as it operates under ambient conditions and produces value-added chemicals.[1–3] Despite widespread interest, achieving high selectivity and efficiency in CO_2 photoreduction remains challenging due to thermodynamic and kinetic limitations.[4–6] The inherent stability of the CO_2 molecule, competitive hydrogen evolution reactions in aqueous environments, limited solar spectrum absorption, and severe charge carrier recombination—especially in single-component systems—further hinder the progress. Thus, developing highly active and selective hybrid photocatalysts is essential.

A promising strategy involves hybrid systems comprising a visible-light-absorbing semiconductor sensitizer and a metal molecular catalyst with high CO_2 reduction activity.[7–23] Recent studies have explored various hybrids, such as ruthenium(II)-complex-modified graphitic carbon nitride (g-C_3N_4) for formate production, and iron (Fe) or cobalt (Co) molecular catalysts coupled with g-C_3N_4, cadmium sulphide (CdS), or related semiconductors for the photoreduction of CO_2 to carbon monoxide (CO).[9–17] In these systems, spatial separation between the light absorber and catalytic centre promotes charge separation and enhances CO_2 reduction performance. Consequently, enhancing both the semiconductor's light-harvesting capacity and its interaction with the molecular catalyst is critical for increasing photon utilization and facilitating electron transfer.[24,25]

Efforts to accelerate electron transfer from photosensitizers to catalysts have led to covalent linker strategies, like direct connection, ethylene or amide bonds;[13,14,26,27] however, these often involve complex synthesis and may suffer from back

[a] CAS Key Laboratory of Green Process and Engineering, Institute of Process Engineering, Chinese Academy of Sciences, Beijing, 100190, China. E-mail: zhanggj@ipe.ac.cn
[b] Key Laboratory of Photochemical Conversion and Optoelectronic Materials, Technical Institute of Physics and Chemistry, Chinese Academy of Sciences, Beijing 100190, China. E-mail: chenyong@mail.ipc.ac.cn
[c] National Center for Nanoscience and Technology, Beijing 100190, China
[d] Zhengzhou Tobacco Research Institute of CNTC, Zhengzhou, 450001, China. E-mail: lib@ztri.com.cn
[e] Department of Chemistry, Johannes Gutenberg University Mainz, Duesbergweg 10-14, 55128 Mainz, Germany
[f] Center of Materials Science and Optoelectronics Engineering, Chinese Academy of Sciences, Beijing, 100049, China

electron transfer, compromising activity and stability. As a covalent bond, a coordination bond can be an ideal intermolecular force to realize the connection between a photosensitizer and a catalyst. The labile nature of coordination bonds confers dynamic stability. At the same time, the coordination interaction is expected to realize inner shell electron transfer, thus overcoming the limitation of diffusion rate and promoting the electron transfer between molecules. Moreover, dynamic coordination interactions offer reversible and self-correcting binding, which can improve the durability of the hybrids.[20]

As an organic semiconductor, g-C_3N_4 has attracted significant attention for various applications due to its facile synthesis, suitable band alignment, good stability, visible-light response and layered structure.[28–32] Nonetheless, pristine g-C_3N_4 suffers from rapid charge recombination and restricted visible-light absorption, limiting its photocatalytic activity. Strategies such as defect engineering, elemental doping, heterojunction construction, and metal deposition have been employed to address these issues.[33–35] Regulating molecular polarity has also emerged as an effective route to promote intramolecular charge transfer and narrow the bandgap of g-C_3N_4.[36–38] Additionally, coupling g-C_3N_4 with molecular catalysts like cobalt phthalocyanine (CoPc)—known for its high selectivity in CO_2-to-CO conversion[39,40]—offers a pathway toward efficient CO_2 reduction, with CO serving as a key industrial feedstock for synthetic fuels and chemicals.

In this work, we introduce polarization engineering and dynamic coordination strategies to enhance the in-plane charge separation in g-C_3N_4 and provide reversible coordination binding sites for CoPc molecular catalyst. Pyridine edge-functionalized g-C_3N_4 (g-C_3N_4-P_x) was designed and synthesized as a light absorber (Scheme S1). The electron-withdrawing pyridine groups can promote the formation of a donor–acceptor structure, narrow the bandgap and improve the visible-light absorption and charge separation. More importantly, the pyridine edges can offer dynamic axial coordination sites for CoPc,[41–43] facilitating interfacial electron transfer from the light-harvesting part, g-C_3N_4, to the catalytic site, CoPc. Through the synergistic effect of polarization engineering and dynamic coordination, efficient charge separation and transfer are realized, and ultimately, the photocatalytic performance of the CoPc/g-C_3N_4-P_x hybrid catalyst for CO_2 reduction is enhanced.

2 Results and discussion

2.1 Structure and morphology

The pyridine edge-functionalized g-C_3N_4-P_x samples were prepared through a facile one-step homogeneous thermal polymerization of urea with different amounts of 4-aminopyridine.[36] A possible polymerization reaction is shown in Scheme S2. Fig. 1a presents the X-ray diffraction (XRD) patterns of pristine g-C_3N_4 and g-C_3N_4-P_x samples, where x is the weight percentage of 4-aminopyridine relative to urea used during synthesis. All XRD patterns exhibit the characteristic diffraction peaks of g-C_3N_4 at 2θ = 12.8° and 27.6°, corresponding to the (100) in-plane structure and the (002) interlayer stacking, respectively. Notably, no significant shift is observed in the positions of these diffraction peaks in the g-C_3N_4-P_x samples compared to pristine g-C_3N_4, indicating that pyridine functionalization at the edges does not alter the crystalline and layered structure of g-C_3N_4. Fig. 1b shows the N_2 adsorption–desorption isotherms of the g-C_3N_4 and g-C_3N_4-P_x samples. All the materials show type IV isotherms with H3 hysteresis, indicative of mesoporous structures. The Brunauer–Emmett–Teller (BET) specific surface areas are measured to be 80.2, 78.0, 75.4, 75.6, 72.7 and 57.6 $m^2\ g^{-1}$ for g-C_3N_4, g-C_3N_4-$P_{0.5}$, g-C_3N_4-$P_{1.0}$, g-C_3N_4-$P_{1.5}$, g-C_3N_4-$P_{2.0}$ and g-C_3N_4-$P_{3.0}$, respectively.

The morphology of pristine g-C_3N_4 and the as-synthesized g-C_3N_4-P_x samples were characterized using scanning electron microscopy (SEM) (Fig. 2a–f) and transmission electron microscopy (TEM) (Fig. 2g–j). All the samples exhibit mesoporous sheet morphology. Specifically, g-C_3N_4, g-C_3N_4-$P_{0.5}$, g-C_3N_4-$P_{1.0}$, and g-C_3N_4-$P_{1.5}$ display predominantly relatively ultrathin, flaky, and porous structures. In contrast, g-C_3N_4-$P_{2.5}$ and g-C_3N_4-$P_{3.0}$—which feature a higher content of edge-grafted pyridine—show increasingly aggregated and thicker sheet-like structures that are less prone to exfoliation. Representative TEM images of g-C_3N_4, g-C_3N_4-$P_{0.5}$, g-C_3N_4-$P_{1.5}$ and g-C_3N_4-$P_{3.0}$ are presented in Fig. 2g–j. These images reveal that g-C_3N_4, g-C_3N_4-

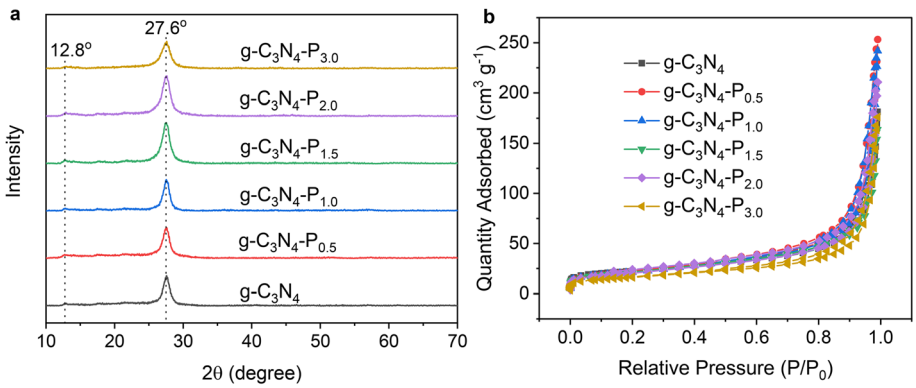

Fig. 1 (a) XRD patterns and (b) N_2 adsorption–desorption isotherms of the pristine g-C_3N_4 and g-C_3N_4-P_x (x = 0.5–3.0) samples.

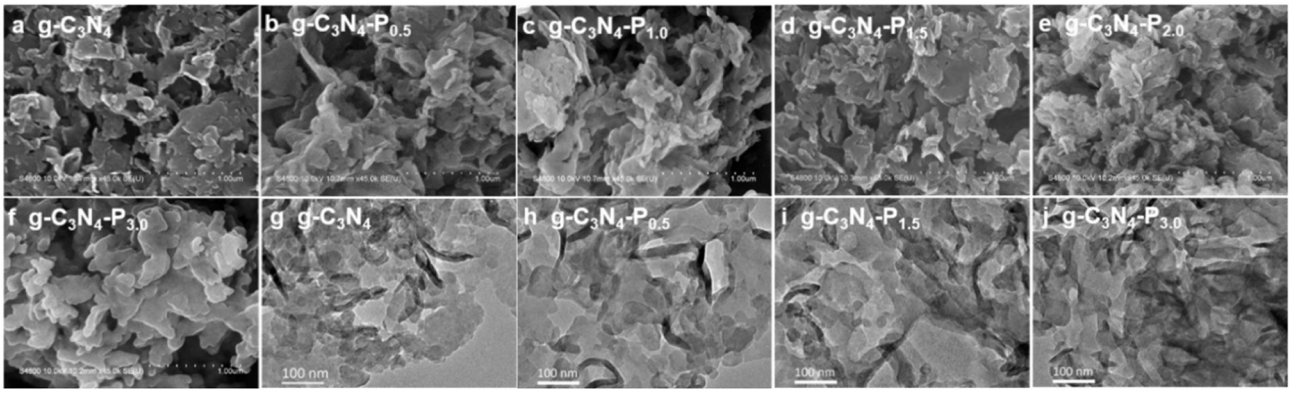

Fig. 2 (a–f) SEM and (g–j) TEM images of the pristine g-C_3N_4 and g-C_3N_4-P_x (x = 0.5–3.0) samples.

$P_{0.5}$ and g-C_3N_4-$P_{1.5}$ maintain a flaky and ultrathin nanosheet structure, whereas g-C_3N_4-$P_{3.0}$ exhibits slightly thicker sheets. Both SEM and TEM results confirm that the edge functionalization with pyridine does not disrupt the fundamental lamellar porous structure of g-C_3N_4, consistent with the XRD patterns shown in Fig. 1a. Samples with low levels of edge-pyridine functionalization (g-C_3N_4-P_x, x = 0–2.0) exhibit relatively high surface areas, attributed to their flaky and porous morphology, which slightly decreases as the degree of pyridine grafting increases. In contrast, g-C_3N_4-$P_{3.0}$, with a high degree of functionalization, shows a marked decrease in surface area (57.6 m^2 g^{-1}), likely due to the formation of thick aggregates, as observed in SEM and TEM images.

The chemical composition and electronic states of the samples were further analysed by X-ray photoelectron spectroscopy (XPS). The XPS survey spectra in Fig. S1a confirm the presence of C and N in all g-C_3N_4-P_x materials, while XPS survey spectra in Fig. S1b confirm the successful hybridisation of CoPc and g-C_3N_4-$P_{1.5}$. The small O peak appearing at 532.1 eV is attributed to the adsorbed H_2O. High-resolution C 1s, N 1s and Co 2p spectra are presented in Fig. S2 and 3a and b, respectively. The C 1s spectrum displays two peaks at 284.8 eV (graphitic carbon, C–C/C═C) and 288.1 eV (sp^2-hybridized carbon in N–C═N/C–N═C groups).[44] The N 1s spectrum can be deconvoluted into three components: pyridinic N (C–N═C) at 398.5–399.6 eV, pyrrolic N (tertiary N–C_3) at 399.8–399.9 eV, and terminal amino groups (–NH_2/NH) at 401.2 eV.[45] While the C 1s spectrum remains unchanged after pyridine modification (Fig. S2), the N 1s peaks corresponding to pyridinic and pyrrolic nitrogen shift slightly to higher binding energy (from 398.5 to 398.7 eV and from 399.8 to 400.1 eV, respectively) after grafting pyridine, suggesting reduced electron density around nitrogen atoms due to the electron-withdrawing effect of grafted pyridine. The Co 2p spectrum displays two peaks at 793.2 eV (Co $2p_{1/2}$) and 777.6 eV (Co $2p_{3/2}$) in CoPc. However, the formation of the CoPc/g-C_3N_4-$P_{1.5}$ hybrid causes the Co $2p_{1/2}$ and Co $2p_{3/2}$ peaks to shift to lower binding energies of 792.4 eV and 776.8 eV, respectively. This indicates an increase in electron density at the Co site because of the electrons flowing from g-C_3N_4-$P_{1.5}$ to CoPc.

2.2 Optical properties and band structures

The optical properties of pristine g-C_3N_4 and the pyridine-modified g-C_3N_4-P_x samples were investigated using UV-vis diffuse reflectance spectroscopy (UV-vis DRS) measurements. As shown in Fig. 4a, the absorption intensity in the visible region initially increases and then decreases, with g-C_3N_4-$P_{1.5}$ exhibiting the strongest absorption between 380 and 450 nm.

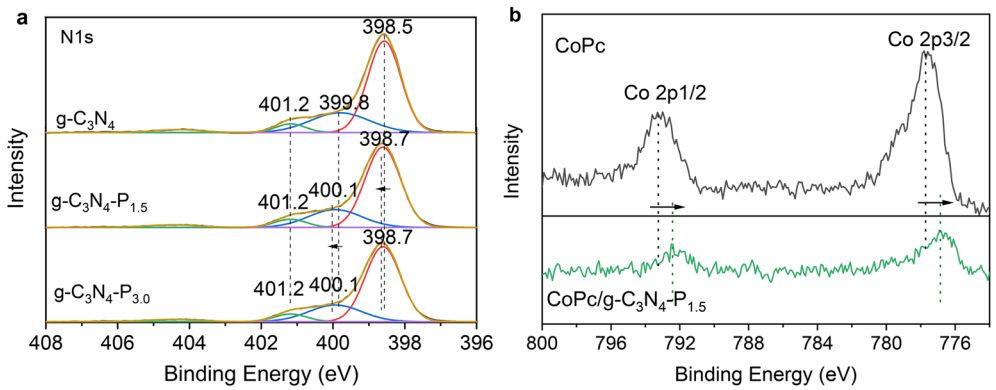

Fig. 3 High-resolution XPS spectra of (a) N 1s of the g-C_3N_4, g-C_3N_4-$P_{1.5}$, and g-C_3N_4-$P_{3.0}$ samples, and (b) Co 2p of CoPc and the CoPc/g-C_3N_4-$P_{1.5}$ hybrid catalyst.

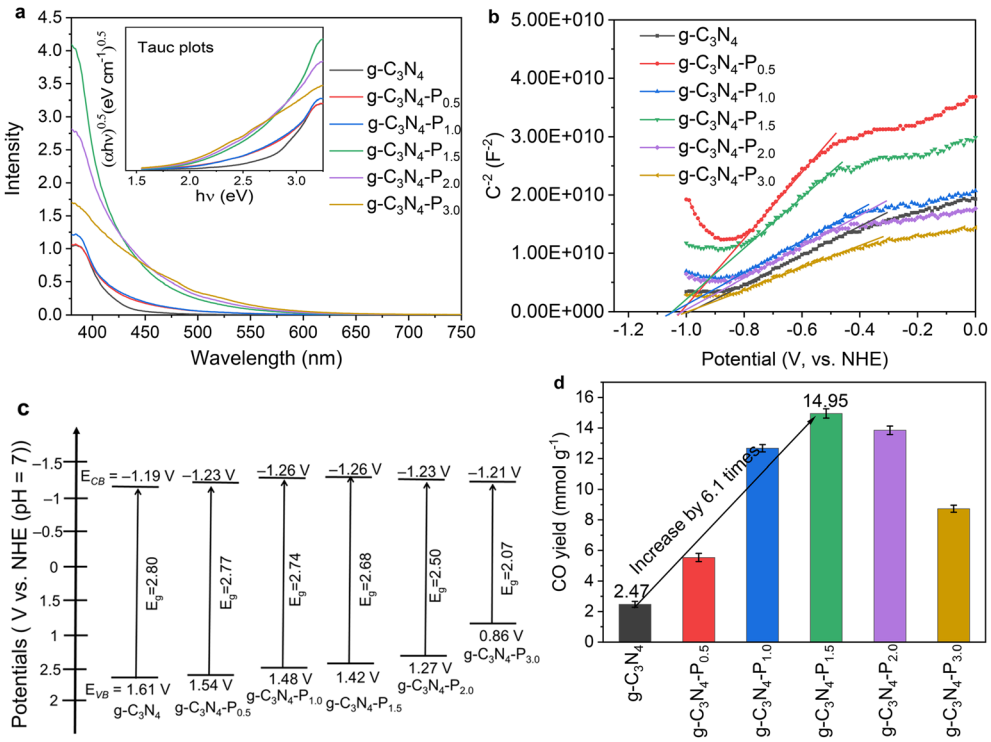

Fig. 4 (a) UV-vis DRS spectra and Tauc plots (inset), (b) Mott–Schottky plots, and (c) band structure alignments for g-C_3N_4 and g-C_3N_4-P_x (x = 0.5–3.0) samples; (d) CO yield from CO_2 photoreduction over g-C_3N_4 and g-C_3N_4-P_x (x = 0.5–3.0) coupled with CoPc in a CH_3CN : H_2O : TEOA (3 : 1 : 1, 100 mL) solution after 6 h of illumination, 420 nm $< \lambda <$ 780 nm), 280 mW cm^{-2}.

Concurrently, the absorption edge progressively red-shifts from g-C_3N_4 to g-C_3N_4-$P_{3.0}$ as the pyridine content increases. Samples g-C_3N_4-$P_{1.5}$, g-C_3N_4-$P_{2.0}$ and g-C_3N_4-$P_{3.0}$ demonstrate significantly enhanced visible-light absorption compared to unmodified g-C_3N_4.

The band gaps (E_g) of the samples, determined *via* the Kubelka–Munk method (Fig. S3), are 2.80 eV (g-C_3N_4), 2.77 eV (g-C_3N_4-$P_{0.5}$), 2.74 eV (g-C_3N_4-$P_{1.0}$), 2.68 eV (g-C_3N_4-$P_{1.5}$), 2.50 eV (g-C_3N_4-$P_{2.0}$), and 2.07 eV (g-C_3N_4-$P_{3.0}$), indicating a gradual narrowing of E_g with increasing pyridine modification. This narrowing band gap is attributed to the formation of an intramolecular donor–acceptor structure within g-C_3N_4-P_x, resulting from the grafting of electron-withdrawing pyridine onto the g-C_3N_4 framework. This structure promotes intramolecular charge separation, thereby causing a red shift in the absorption edge and enhancing visible-light absorption. Consistent with these changes, the powder colour deepens from light yellow to dark yellow with increasing pyridine content, as shown in Fig. S4.

Mott–Schottky measurements were conducted to determine the flat-band potentials (E_{FB}) of the synthesized g-C_3N_4 and g-C_3N_4-P_x samples. As shown in Fig. 4b, the positive slopes of the Mott–Schottky plots confirm that all samples exhibit n-type semiconductor behaviour. The E_{FB} values were obtained by extrapolating the linear region of the plots to the intercept on the x-axis (where $1/C^2 = 0$).[46,47] The calculated E_{FB} values are −0.99, −1.03, −1.06, −1.06, −1.03 and −1.01 V (*vs.* the normal hydrogen electrode, NHE) for g-C_3N_4, g-C_3N_4-$P_{0.5}$, g-C_3N_4-$P_{1.0}$, g-C_3N_4-$P_{1.5}$, g-C_3N_4-$P_{2.0}$, and g-C_3N_4-$P_{3.0}$, respectively. For n-type semiconductors, the conduction band minimum (E_{CB}) is typically 0.1–0.3 eV higher than E_{FB}, depending on the electron effective mass and carrier concentration.[48,49] Assuming a difference of 0.2 eV, the estimated E_{CB} values are −1.19 V, −1.23 V, −1.26 V, −1.26 V, −1.23 V, and −1.21 V (*vs.* NHE) for g-C_3N_4, g-C_3N_4-$P_{0.5}$, g-C_3N_4-$P_{1.0}$, g-C_3N_4-$P_{1.5}$, g-C_3N_4-$P_{2.0}$, and g-C_3N_4-$P_{3.0}$, respectively. The Mott–Schottky results indicate that pyridine modification at the edges has a minimal effect on both E_{FB} and E_{CB} of the g-C_3N_4-P_x materials.

Based on the E_g values derived from the Tauc plots in Fig. 4a, the valence band energy (E_{VB}) values of g-C_3N_4, g-C_3N_4-$P_{0.5}$, g-C_3N_4-$P_{1.0}$, g-C_3N_4-$P_{1.5}$, g-C_3N_4-$P_{2.0}$ and g-C_3N_4-$P_{3.0}$ were calculated to be 1.61, 1.54, 1.48, 1.42, 1.27, and 0.86 V (*vs.* NHE), respectively. This progressive increase in E_{VB} indicates that pyridine incorporation at the edges of the g-C_3N_4 framework systematically increases the valence band level. As depicted in the band structure diagram in Fig. 4c, pyridine modification leads to a continuous reduction of the band gap from 2.80 eV to 2.07 eV, accompanied by an upward shift of the E_{VB} from 1.61 eV to 0.86 eV. In contrast, the conduction band level remains essentially unchanged, with E_{CB} values confined within a narrow range of −1.19 V to −1.26 V—a variation of only 0.02–0.07 V across all samples. This stability in the conduction band preserves the original charge transfer direction while concurrently suppressing carrier recombination. Although narrow-bandgap semiconductors typically exhibit high charge recombination rates, this work

demonstrates an effective strategy for significantly narrowing the band gap without compromising charge separation efficiency.

2.3 Photoreduction of CO_2 over CoPc/g-C_3N_4-P_x hybrid catalysts

First, a series of control experiments was conducted to confirm that the observed products originate exclusively from the photoreduction of CO_2. These experiments were conducted under an argon (Ar) atmosphere rather than CO_2, in the dark without illumination, using only CoPc (without a photosensitizer), using only g-C_3N_4-P_x (without CoPc), and without any hybrid photocatalyst. Table S1 lists the results of the corresponding control experiments for CO_2 photoreduction based on the CoPc/g-C_3N_4-$P_{1.5}$ hybrid catalyst. No product was detected under an argon atmosphere, in the dark, in the absence of the CoPc/g-C_3N_4-P_x hybrid catalyst, or with only CoPc (without a photosensitizer). Only trace CH_4 was detected with only g-C_3N_4-P_x (without CoPc) under visible-light irradiation. These results confirm that the CO originates from the photoreduction of CO_2 catalysed by the CoPc/g-C_3N_4-P_x hybrid catalyst, and CoPc itself (without a sensitizer) has no activity for CO_2 reduction under visible-light irradiation.

Under visible-light illumination (420 nm $< \lambda <$ 780 nm), the prepared CoPc/g-C_3N_4-P_x hybrid catalysts show high photocatalytic activity and selectivity for CO_2 reduction to CO, attributed to the intrinsic CO selectivity of CoPc. Only CO was detected, no CH_4, H_2, C_2 gas, or liquid products in CO_2 reduction based on the CoPc/g-C_3N_4-P_x hybrid photocatalyst were detected. The order of performance under visible light was as follows: CoPc/g-C_3N_4-$P_{1.5}$ (14.95 mmol g^{-1}) > CoPc/g-C_3N_4-$P_{2.0}$ (13.85 mmol g^{-1}) > CoPc/g-C_3N_4-$P_{1.0}$ (12.67 mmol g^{-1}) > CoPc/g-C_3N_4-$P_{3.0}$ (8.73 mmol g^{-1}) > CoPc/g-C_3N_4-$P_{0.5}$ (5.54 mmol g^{-1}) > CoPc/g-C_3N_4 (2.47 mmol g^{-1}) after 6 hours. The highest CO yield of 14.95 mmol g^{-1} was achieved with the CoPc/g-C_3N_4-$P_{1.5}$ catalyst, which is approximately 6.1 times that of the unmodified CoPc/g-C_3N_4. When pyridine was grafted onto the g-C_3N_4 framework, the CO yield initially increased significantly with increasing pyridine content. Further increasing the pyridine grafting amount resulted in a decrease in the photocatalytic activity. Table S2 lists the recent advances in the photocatalytic reduction of CO_2 based on molecular catalyst/semiconductor hybrid photocatalysts, and the CoPc/g-C_3N_4-$P_{1.5}$ hybrid catalyst exhibits competitive performance, especially in terms of CO yield based on non-noble metal molecular/g-C_3N_4 hybrid catalysts under visible-light irradiation.

To evaluate the superior stability of the CoPc/g-C_3N_4-$P_{1.5}$ hybrid catalyst compared to the unmodified CoPc/g-C_3N_4, a continuous 12-hour CO_2 photoreduction test was conducted. As shown in Fig. S6, the time-dependent CO evolution was monitored using two catalytic systems: 50 mg of g-C_3N_4-$P_{1.5}$ hybrid with 1.0 mg of CoPc, and 50 mg of g-C_3N_4 hybrid with 1.0 mg of CoPc, both dispersed in an acetonitrile/water/triethanolamine (CH_3CN/H_2O/TEOA) mixed solution (3 : 1 : 1, 100 mL) under visible-light irradiation. The CO yield from the CoPc/g-C_3N_4-$P_{1.5}$ catalyst increased almost linearly over 12 hours, demonstrating significantly higher efficiency and durability than CoPc/g-C_3N_4. These results confirm the excellent stability of the CoPc/g-C_3N_4-$P_{1.5}$ hybrid under visible-light conditions. Notably, the dynamic coordination bond in the CoPc/g-C_3N_4-$P_{1.5}$ hybrid interface confers a certain self-repairing capability, thereby enhancing the overall durability of the catalytic system.

2.4 Mechanism of the enhanced photocatalytic performance

2.4.1 EIS Nyquist plots and transient photocurrent response. To elucidate the enhanced photocatalytic performance, electrochemical impedance spectroscopy (EIS) Nyquist plots and transient photocurrent–time response (*I–t*) curves were recorded using g-C_3N_4 and g-C_3N_4-P_x films as working electrodes. EIS reflects the charge transfer resistance at the electrode/electrolyte interface, while the *I–t* curves provide further insight into the synergistic effect of light absorption and photo-generated charge separation. The impedance parameters can be derived from the spectra using an equivalent circuit shown in the inset in Fig. 5a. In the equivalent circuit, R_{ct} corresponds to the charge transfer impedance. The R_{ct} values of g-C_3N_4, g-C_3N_4-$P_{0.5}$, g-C_3N_4-$P_{1.0}$, g-C_3N_4-$P_{1.5}$, g-C_3N_4-$P_{2.0}$ and g-C_3N_4-$P_{3.0}$ were fitted to be 2394, 1738, 761, 759, 768, and 1377 Ω, respectively. The R_{ct} value decreases significantly from g-C_3N_4 to g-C_3N_4-$P_{1.5}$, and then gradually increases from g-C_3N_4-$P_{2.0}$ to g-C_3N_4-$P_{3.0}$. The smallest radius is observed for g-C_3N_4-$P_{1.5}$, and accordingly, g-C_3N_4-$P_{1.5}$ shows the lowest R_{ct} value and, therefore, the lowest charge transfer resistance and most efficient charge separation, which correlates well with the CO_2 photoreduction activity shown in Fig. 4d and is further supported by the transient photocurrent results below. These findings suggest that appropriate incorporation of pyridine significantly facilitates charge separation and transfer.

Moreover, under visible-light irradiation, all pyridine-modified samples (g-C_3N_4-P_x) exhibit substantially higher photocurrents than pristine g-C_3N_4 (Fig. 5b). As indicated in Fig. 4a, the enhanced visible-light absorption resulting from pyridine grafting contributes to the improved photocurrent response. The photocurrent increases progressively from g-C_3N_4 to g-C_3N_4-$P_{1.5}$, and then decreases from g-C_3N_4-$P_{1.5}$ to g-C_3N_4-$P_{3.0}$. The trend in photocurrent intensity aligns closely with the photocatalytic CO production performance (Fig. 4d), with minor discrepancies observed for g-C_3N_4-$P_{1.0}$ and g-C_3N_4-$P_{3.0}$. Among all the samples, g-C_3N_4-$P_{1.5}$ demonstrates the highest photocurrent, implying optimal synergy between light harvesting and charge separation. Therefore, appropriate edge-grafting of pyridine is an effective strategy for enhancing the photoelectrochemical properties of g-C_3N_4.

2.4.2 Steady-PL and TR-PL kinetics decay. Steady-state and time-resolved photoluminescence (steady-PL and TR-PL) decay spectra were acquired with excitation at 370 nm and emission monitored at 460 nm to probe the charge carrier dynamics within the materials. As presented in Fig. 6a, both pristine g-C_3N_4 and pyridine-edge-functionalized g-C_3N_4-P_x samples

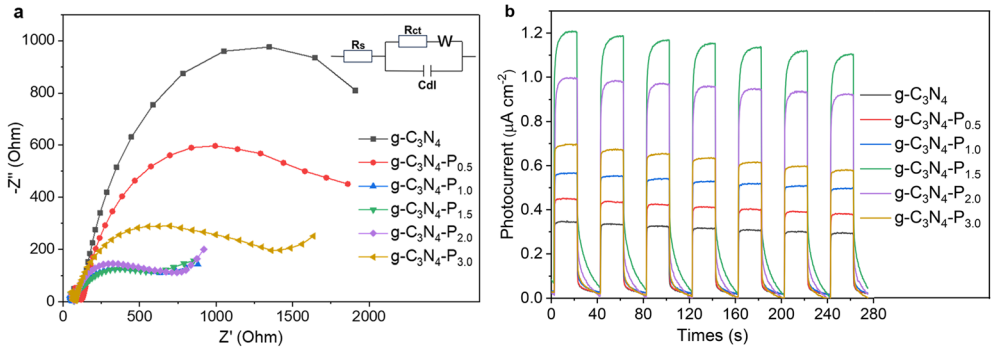

Fig. 5 (a) EIS Nyquist plots (the inset shows the equivalent circuit), and (b) the transient photocurrent response (*I*–*t*) of the pristine g-C_3N_4 and g-C_3N_4-P_x (*x* = 0.5–3.0) samples.

exhibit a broad fluorescence emission band. The pristine g-C_3N_4 demonstrates the highest emission intensity, indicative of strong radiative charge recombination. A notable quenching of the steady-PL intensity is observed across all pyridine-modified samples, particularly from g-C_3N_4-$P_{1.0}$ onward. This suppression implies significantly reduced radiative recombination, which we attribute to facilitated electron transfer *via* non-radiative pathways and enhanced charge separation resulting from pyridine grafting. The introduction of pyridine moieties at the framework edges likely provides charge delocalization channels and promotes interfacial electron transfer, thereby suppressing recombination.

Concurrently, a systematic red shift in the emission peak from 453 nm (g-C_3N_4) to 570 nm (g-C_3N_4-$P_{3.0}$) is observed with increasing pyridine content. This red-shift reflects a narrowing of the effective bandgap due to the formation of an intramolecular donor–acceptor (D–A) structure, wherein the electron-donating triazine units interact with the electron-accepting pyridine on the edge of g-C_3N_4. The variation trend of the red shift in the PL emission peak aligns well with the red shift of the absorption onset shown in Fig. 4a, corroborating the electronic modulation of the material through functionalization. These PL results collectively affirm that pyridine edge-grafting effectively alters the electronic structure of g-C_3N_4, facilitating charge separation and transfer—key factors underlying the enhanced photocatalytic performance.

The TR-PL decay spectra monitored at 460 nm (Fig. 6b) provide further insight into the charge transfer dynamics. All samples exhibit typical exponential decay behaviour, with the pyridine-modified g-C_3N_4-P_x samples demonstrating markedly accelerated decay kinetics compared to pristine g-C_3N_4. Moreover, a progressive acceleration in PL decay is observed from g-C_3N_4-$P_{0.5}$ to g-C_3N_4-$P_{3.0}$. The fluorescence lifetimes were quantitatively analysed using a tri-exponential decay model, and the fitted results are summarized in Table 1. Each lifetime component (τ_1, τ_2 and τ_3) exhibits a consistent decreasing trend with increasing pyridine content. The average fluorescence lifetime (τ_{av}) decreases sequentially from 6.11 ns (pristine g-C_3N_4) to 1.84 ns (g-C_3N_4-$P_{3.0}$), confirming enhanced non-radiative decay pathways.

This systematic reduction in lifetime reflects more efficient electron transfer from the g-C_3N_4 matrix to the pyridine functional groups at the material's edge. The introduced pyridine rings serve as electron-accepting sites, facilitating rapid separation and extraction of photo-generated electrons, thereby suppressing radiative recombination. Together, the steady-state and time-resolved PL results conclusively demonstrate that pyridine edge functionalization promotes the separation of photoinduced electron–hole pairs and inhibits their recombination.

2.4.3 Theoretical calculation. To gain deeper mechanistic insights into how pyridine edge-grafting enhances the photocatalytic performance and charge separation in g-C_3N_4-

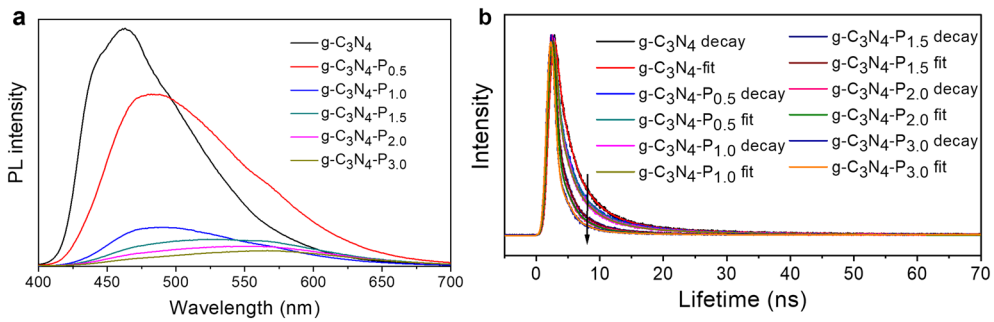

Fig. 6 (a) Steady-PL and (b) TR-PL kinetics decay spectra probed at 460 nm for the pristine g-C_3N_4 and as-synthesized g-C_3N_4-P_x (*x* = 0.5–3.0) samples at 370 nm excitation.

Table 1 The fitted parameters for the fluorescence lifetime of the as-synthesized g-C_3N_4-P_x (x = 0–3.0) sample

	g-C_3N_4	g-C_3N_4-$P_{0.5}$	g-C_3N_4-$P_{1.0}$	g-C_3N_4-$P_{1.5}$	g-C_3N_4-$P_{2.0}$	g-C_3N_4-$P_{3.0}$
τ_1 (ns)	4.03	3.70	3.40	2.66	2.58	2.07
Rel.%	52.03%	44.61%	43.25%	39.82%	36.82%	31.59%
τ_2 (ns)	16.67	14.51	12.90	11.1	11.19	8.81
Rel.%	22.33%	25.27%	24.72%	15.86%	12.58%	11.07%
τ_3 (ns)	1.14	0.82	0.71	0.51	0.48	0.36
Rel.%	25.64%	30.12%	32.04%	44.32%	50.60%	57.34%
τ (ns)	6.11	5.56	4.89	3.05	2.60	1.84

P_x, density functional theory (DFT) calculations were performed to evaluate the molecular dipole moment and the electron density distribution of the highest occupied molecular orbitals (HOMOs) and the lowest unoccupied molecular orbitals (LUMOs). The molecular model of g-C_3N_4 was constructed using three connected 3-*s*-triazine units, while the g-C_3N_4-P_x model was built by grafting one pyridine ring onto the terminal triazine unit. As shown in Fig. 7, the optimized structures, computed dipole moments, and spatial distributions of the HOMO and LUMO are compared for g-C_3N_4 and g-C_3N_4-P_x. The dipole moment increases from 4.75 debye in g-C_3N_4 to 5.47 debye in g-C_3N_4-P_x, indicating enhanced molecular polarity induced by pyridine functionalization. This greater polarity facilitates improved charge separation and promotes more efficient charge transport within the material.

Orbital analysis in Fig. 7 reveals that in pristine g-C_3N_4, the HOMO is delocalized evenly across all three triazine units, whereas the LUMO is predominantly localized on two of the triazine units. In contrast, for g-C_3N_4-P_x, the HOMO is mainly distributed over the two triazine units distal to the pyridine group, with minimal contribution from the pyridine-linked triazine and none from the pyridine itself. The LUMO, however, is primarily located on the pyridine-anchored triazine unit, with additional density extending into the pyridine ring and the remaining triazine motifs. The frontier molecular orbitals, the HOMO and LUMO, correspond to bonding and anti-bonding orbitals, respectively, and dictate the spatial distribution of holes and electrons upon photoexcitation. Compared with pristine g-C_3N_4, the isodensity surface plots of g-C_3N_4-P_x reveal a more pronounced and directional shift of electron density from the 3-*s*-triazine core toward the edge-anchored pyridine ring under excitation. This redistribution supports efficient photoinduced electron transfer from the central region to the peripheral functional groups, thereby facilitating charge separation and reducing the likelihood of electron–hole recombination. The DFT simulation results align consistently with the fluorescence spectra discussed above.

2.4.4 Mechanism of the optimum photocatalytic performance at $P_{1.5}$. Thermodynamically, all g-C_3N_4-P_x samples can transfer electrons to CoPc [E_{CB} for g-C_3N_4-P_x = −1.19 to −1.26 V *vs.* NHE; $E_{red(CoPc)} \approx$ −0.90 V *vs.* NHE,[50] satisfying the requirement for CO_2 reduction ($E_{(CO_2/CO)}$ = −0.52 V *vs.* NHE)]. The slight variation in E_{CB} (0.02–0.07 eV) among g-C_3N_4-P_x samples implies negligible differences in driving force for electron transfer, indicating that the enhanced activity does not originate from thermodynamic factors. A charge transfer diagram for CO_2 photoreduction over CoPc/g-C_3N_4-P_x hybrid catalysts is proposed, as shown in Scheme 1. First, photoexcitation of g-C_3N_4-P_x generates electron–hole pairs; second, electrons transfer efficiently to CoPc *via* pyridine bridges, while holes migrate to the g-C_3N_4-

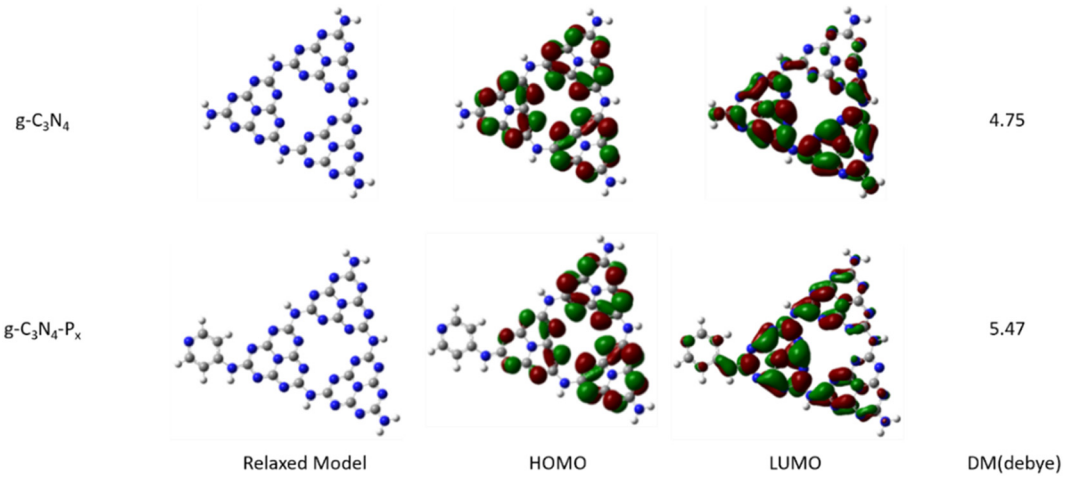

Fig. 7 Optimized structures, calculated dipole moments, and isodensity surface plots of the HOMO and LUMO for g-C_3N_4 and g-C_3N_4-P_x model structures.

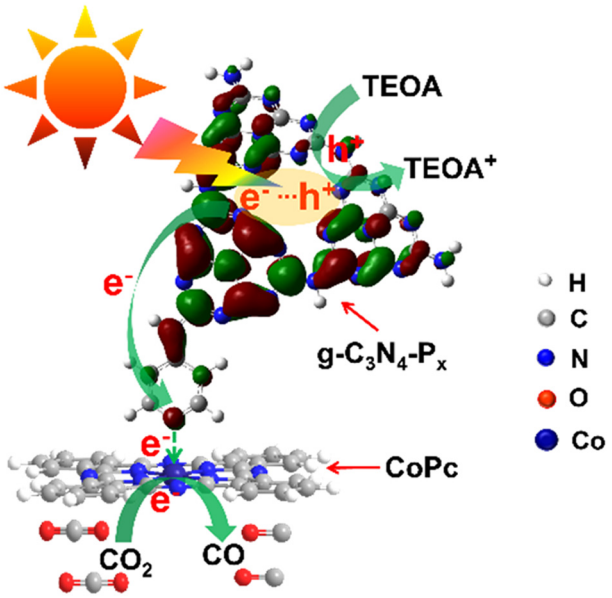

Scheme 1 Charge transfer diagram for CO_2 photoreduction over CoPc/g-C_3N_4-P_x hybrid photocatalysts under visible-light illumination.

P_x surface, competing with recombination; finally, CO_2 is reduced to CO at CoPc sites, while the holes are scavenged by the sacrificial agent TEOA. As shown in Fig. 4d, the photocatalytic activity of CoPc/g-C_3N_4-P_x depends strongly on the pyridine grafting level (x). The CO_2 reduction performance increases with pyridine loading up to an optimum level at x = 1.5, beyond which it declines. This trend can be explained by the interplay of several key factors.

The optimum performance at $P_{1.5}$ reflects a kinetic spot between enhanced charge separation and competing recombination pathways. At lower loadings ($x < 1.5$), increasing pyridine content improves visible-light absorption, facilitates in-plane charge separation within g-C_3N_4, and promotes directional electron transfer from g-C_3N_4-P_x to CoPc. This is supported by the lowest charge-transfer resistance (Fig. 5a) and highest photocurrent response (Fig. 5b) observed at $P_{1.5}$. However, further increasing the pyridine loading beyond this point introduces excess surface defects or states that act as charge recombination centres, as indicated by the increased charge-transfer resistance and decreased photocurrent. These defects promote electron–hole recombination before electrons can reach the CoPc active sites. In addition, excess pyridine functionalization leads to an overly elevated valence band maximum (E_{VB} in Fig. 4c), which reduces the hole oxidation power and weakens the oxidative half-reaction, thereby impairing catalyst regeneration. Moreover, while the optimal pyridine content enables efficient coordination and electron transfer to CoPc, an excess may cause non-productive coordination or steric hindrance, blocking active sites and leading to local electron accumulation. This imbalance between pyridine and CoPc promotes recombination instead of catalysis, ultimately reducing the CO_2 reduction efficiency.[51,52]

3 Conclusions

In conclusion, we successfully synthesized pyridine edge-functionalized g-C_3N_4-P_x coupled with CoPc for efficient photocatalytic CO_2 reduction to CO under visible light. In this hybrid system, g-C_3N_4-P_x serves as the light-harvesting unit, while CoPc acts as the catalytic site for CO_2 reduction. The grafting of electron-withdrawing pyridine groups enhances visible-light absorption and promotes directional in-plane charge separation within g-C_3N_4. Unlike conventional CoPc/g-C_3N_4 systems, which primarily rely on physical adsorption, static interactions, or direct covalent linking, our work introduces polarization engineering and coordination *via* pyridine edge functionalization. This approach not only promotes in-plane charge separation within g-C_3N_4, for improved light absorption, but also enables directional electron transfer and reversible coordination between g-C_3N_4 and CoPc, significantly increasing charge separation and CO_2 reduction performance. The optimal catalyst, CoPc/g-C_3N_4-$P_{1.5}$, achieves a CO yield of 14.95 mmol g^{-1} after 6 h of visible-light irradiation, which is 6.1 times that of the non-functionalized counterpart. The improvement in the photocatalytic activity is mainly due to the increase in the electron velocity between the photosensitizer and catalyst, which emphasizes the superiority of directional electron transfer and the construction of a dynamic coordination interaction. The one-step thermal polymerization used for g-C_3N_4-P_x is simple, scalable, and based on low-cost precursors, and the coordination with CoPc is also straightforward and conducted under mild conditions, making the CoPc/g-C_3N_4-P_x hybrid suitable for large-scale production. This work offers strategic guidelines for designing efficient semiconductor–molecular hybrid photocatalysts for CO_2 conversion into solar fuel.

4 Experimental

4.1 Regents

All the reagents and solvents were chromatographic or analytical grade. Urea, 4-aminopyridine, TEOA, CH_3CN, and *N*, *N*-dimethylformamide (DMF) were purchased from Shanghai Aladdin Bio-chem Technology. Tetraethylammonium tetrafluoroborate (Et_4NBF_4) was obtained from Sigma-Aldrich. CO_2 with a purity of 99.999% was bought from Shanxi Beiwen Gases Company. Ultrapure water (Millipore Milli-Q grade, 18.2 MΩ cm) was used in all the experiments.

4.2 Synthesis

Pristine g-C_3N_4 was synthesized by direct thermal polymerization of urea at 560 °C for 4 h with a heating rate of 2.5 °C min^{-1} in a lidded alumina crucible in a muffle furnace under an ambient atmosphere. The pyridine edge-functionalized g-C_3N_4-P_x samples were prepared through thermal polymerization of urea with different amounts of 4-aminopyridine, as for the synthetic process of g-C_3N_4. The edge-grafted amount of pyridine in the final g-C_3N_4-P_x composites was controlled by varying the quantity of 4-aminopyridine used in the thermal polymerization. The g-

C_3N_4-P_x samples synthesized with 4-aminopyridine to urea weight percentages of 0.5%, 1.0%, 1.5%, 2.0%, and 3.0% were denoted as g-C_3N_4-$P_{0.5}$, g-C_3N_4-$P_{1.0}$, g-C_3N_4-$P_{1.5}$, g-C_3N_4-$P_{2.0}$, and g-C_3N_4-$P_{3.0}$, respectively.

CoPc was synthesized and characterized as previously reported.[53] The CoPc/g-C_3N_4-P_x hybrid catalysts were prepared by mixing 1 mg of CoPc with 50 mg of g-C_3N_4-P_x under stirring overnight in a 100 mL solution of CH_3CN/H_2O/TEOA (3 : 1 : 1, v : v : v). FT-IR spectra were recorded to verify the CoPc/g-C_3N_4-$P_{1.5}$ heterogeneous catalyst (Fig. S5).

4.3 Characterization

The morphology of the g-C_3N_4-P_x samples was observed on a Hitachi S4800 field emission SEM and FEI Tecnai G2 T20 TEM. XRD was measured on a Bruker D8 diffractometer with Cu Kα radiation. The BET specific surface area was measured by a surface area and porosity analyser (Micromeritics, TriStar II 3020). XPS was carried out on an ESCALAB 250Xi X-ray photoelectron spectrometer. UV-vis DRS was recorded on a Lambda 750 UV/vis/NIR spectrophotometer (Perkin-Elmer, USA) using $BaSO_4$ as the background. Steady-state PL and TR-PL decay spectra with excitation at 370 nm were collected on a NanoLOG-TCSPC spectrophotometer (Horiba Jobin Yvon, USA). Transient *I–t* curves and Mott–Schottky plots were tested with a frequency of 1 kHz. EIS measurements were performed under an AC amplitude of 10 mV with a frequency range of 10^{-1} Hz to 10^5 Hz. All of the photoelectrochemical measurements were performed in a three-electrode cell on a CHI 660D potentiostat (Shanghai Chenhua) in DMF solution using 0.1 M Et_4NBF_4 as the electrolyte. g-C_3N_4-P_x films on FTO glass, Pt sheet and Ag/AgCl were used as working, counter and reference electrodes, respectively.

4.4 Photocatalytic CO_2 reduction

Photoreduction of CO_2 was performed over CoPc/g-C_3N_4-P_x hybrid photocatalysts in a CH_3CN/H_2O/TEOA (3 : 1 : 1, 100 mL) mixed solution in a photoreaction system (Labsolar-IIIAG, Beijing Perfectlight Technology Co., Ltd.) saturated with 28 kPa of CO_2 at 15 °C, as reported.[11] The volume of the reactor was 250 mL, and the volume of the gas circulation pipeline was 150 mL. The photoreaction system was vacuumed and purged with high-purity CO_2 gas for 1 h before illumination. The reactor was illuminated under visible light ($420\ nm < \lambda < 780\ nm$) using a 300 W Xe lamp (Microsolar 300, Beijing Perfectlight Technology Co., Ltd.) with a 420 nm cut-off filter and a 780 nm IR-cut filter. The spot diameter is 60 mm, and the irradiation height is 10 cm. The light intensity was calibrated using a silicon photodiode power meter, with 280 mW cm^{-2}. The total photon flux was calculated to be approximately 1.26×10^{-6} photons per s m^{-2}. The spectrum of Microsolar 300 Xe light ($420\ nm < \lambda < 780$ nm) is shown in Fig. S7. The gas reduction products were analysed by using an Agilent 7890A gas chromatograph equipped with a hydrogen flame ionization detector (FID) and a thermal conductivity detector (TCD) using He as the carrier gas. The FID was fitted with a methanizer to detect CO. Typical chromatographic curves of CH_4 and CO with residence times and GC calibration curves are shown in Fig. S8 and S9, respectively. A series of control experiments (*i.e.*, purging Ar instead of CO_2, in the dark without illumination, with only CoPc and without the photosensitizer, with only g-C_3N_4-P_x and without CoPc, and without the hybrid photocatalyst) were carried out.

4.5 Theoretical calculation

Theoretical calculation was carried out using Gaussian software using the DFT method.[54] Becke's three-parameter hybrid functional with the LYP correlation functional (B3LYP) together with the 6-31G(d) basis set was employed. Geometry optimization and electronic property analysis of the g-C_3N_4 and g-C_3N_4-P_x models with the minimum energy conformation were carried out without any symmetry constraint. The molecular dipole moment and electron distribution of the HOMO and LUMO were obtained.

Author contributions

Xuehua Zhang: resources, methodology, formal analysis, data curation, writing – original draft. Chunlei Su: resources, formal analysis, data curation. Rui Shi: data curation. Mingming Li: methodology. Lili Fu: formal analysis. Rongji Liu: methodology, investigation. Yong Chen: writing – review & editing, visualization, validation. Bin Li: formal analysis, review & editing, funding acquisition. Guangjin Zhang: formal analysis, writing – review & editing, supervision, funding acquisition and project administration.

Conflicts of interest

The authors declare no conflict of interest.

Data availability

The data supporting this article have been included as part of the supplementary information (SI).

Supplementary information: the model structure unit of CoPc/g-C_3N_4-P_x hybrid photocatalysts; the possible synthetic scheme of g-C_3N_4-P_x; XPS survey spectra of g-C_3N_4, g-C_3N_4-P_x, CoPc and CoPc/g-C_3N_4-$P_{1.5}$ hybrid, XPS spectra of C1s and N1s of g-C_3N_4 and g-C_3N_4-P_x; Tauc plots and photographs of g-C_3N_4 and g-C_3N_4-P_x; IR spectra of g-C_3N_4-$P_{1.5}$, CoPc and CoPc/g-C_3N_4-$P_{1.5}$ hybrid; time dependence of CO evolution based on CoPc/g-C_3N_4 and CoPc/g-C_3N_4-P_x in 12 h; the out spectrum of Microsolar 300 Xe light; typical chromatographic curves of CH_4 and CO and GC calibration curves; results of the corresponding control experiments for CO_2 photoreduction and recent advances of CO_2 photoreduction based on molecular catalyst/semiconductor hybrid photocatalysts. See DOI: https://doi.org/10.1039/d5im00296f.

Acknowledgements

This work is supported by the National Natural Science Foundation of China (22378402; 22178361), the International Partnership Project of CAS (039GJHZ2022029GC), Fundamental research project of China National Tobacco Corporation (No. 110202403002) and the Major Project of the Innovation Platform at the Key Laboratory of Tobacco Processing Technology, State Tobacco Monopoly Administration (CNTC, 202025AWCX01).

References

1 T. Inoue, A. Fujishima, S. Konishi and K. Honda, Photoelectrocatalytic reduction of carbon dioxide in aqueous suspensions of semiconductor powders, *Nature*, 1979, **277**, 637–638.

2 W. Tu, Y. Zhou and Z. Zou, Photocatalytic conversion of CO_2 into renewable hydrocarbon fuels: State-of-the-art accomplishment, challenges, and prospects, *Adv. Mater.*, 2014, **26**, 4607–4626.

3 X. Li, J. Yu, M. Jaroniec and X. Chen, Cocatalysts for selective photoreduction of CO_2 into solar fuels, *Chem. Rev.*, 2019, **119**, 3962–4179.

4 Y. Wang, E. Chen and J. Tang, Insight on reaction pathways of photocatalytic CO_2 conversion, *ACS Catal.*, 2022, **12**, 7300–7316.

5 C. Huang, X. Zhang, D. Li, M. Wang and Q. Wu, The influence of the precursor molar ratio on the structure of the CdS catalyst during synthesis and visible-light driven CO_2 reduction into solar fuel, *New J. Chem.*, 2022, **46**, 10339–10346.

6 D. Zhang and H. Wang, Polyoxometalate-based nanostructures for electrocatalytic and photocatalytic CO_2 reduction, *Polyoxometalates*, 2022, **1**, 9140006.

7 T. Morikawa, S. Sato, K. Sekizawa, T. Suzuki and T. Arai, Solar-driven CO_2 reduction using a semiconductor/molecule hybrid photosystem: From photocatalysts to a monolithic artificial leaf, *Acc. Chem. Res.*, 2022, **55**, 933–943.

8 S. Zhang, R. Liu, C. Streb and G. Zhang, Design and synthesis of novel polyoxometalate-based binary and ternary nanohybrids for energy conversion and storage, *Polyoxometalates*, 2023, **2**, 9140037.

9 R. Kuriki, K. Sekizawa, O. Ishitani and K. Maeda, Visible-light-driven CO_2 reduction with carbon nitride: Enhancing the activity of ruthenium catalysts, *Angew. Chem., Int. Ed.*, 2015, **54**, 2406–2409.

10 G. Zhao, H. Pang, G. Liu, P. Li, H. Liu, H. Zhang, L. Shi and J. Ye, Co-porphyrin/carbon nitride hybrids for improved photocatalytic CO_2 reduction under visible light, *Appl. Catal., B*, 2017, **200**, 141–149.

11 L. Lin, C. Hou, X. Zhang, Y. Wang, Y. Chen and T. He, Highly efficient visible-light driven photocatalytic reduction of CO_2 over g-C_3N_4 nanosheets/tetra(4-carboxyphenyl) porphyrin iron(III) chloride heterogeneous catalysts, *Appl. Catal., B*, 2018, **221**, 312–319.

12 X. Zhang, L. Lin, D. Qu, J. Yang, Y. Weng, Z. Wang, Z. Sun, Y. Chen and T. He, Boosting visible-light driven solar-fuel production over g-C_3N_4/tetra(4-carboxyphenyl)porphyrin iron(III) chloride hybrid photocatalyst via incorporation with carbon dots, *Appl. Catal., B*, 2020, **265**, 118595.

13 B. Ma, G. Chen, C. Fave, L. Chen, R. Kuriki, K. Maeda, O. Ishitani, T.-C. Lau, J. Bonin and M. Robert, Efficient visible-light-driven CO_2 reduction by a cobalt molecular catalyst covalently linked to mesoporous carbon nitride, *J. Am. Chem. Soc.*, 2020, **142**, 6188–6195.

14 Y. Wei, L. Chen, H. Chen, L. Cai, G. Tan, Y. Qiu, Q. Xiang, G. Chen, T.-C. Lau and M. Robert, Highly efficient photocatalytic reduction of CO_2 to CO by in situ formation of a hybrid catalytic system based on molecular iron quaterpyridine covalently linked to carbon nitride, *Angew. Chem., Int. Ed.*, 2022, **61**, e202116832.

15 P. Li, C. Hou, X. Zhang, Y. Chen and T. He, Ethylenediamine-functionalized CdS/tetra(4-carboxyphenyl) porphyrin iron (III) chloride hybrid system for enhanced CO_2 photoreduction, *Appl. Surf. Sci.*, 2018, **459**, 292–299.

16 P. Li, X. Zhang, C. Hou, L. Lin, Y. Chen and T. He, Visible-light-driven CO_2 photoreduction over $Zn_xCd_{1-x}S$ solid solution coupling with tetra(4-carboxyphenyl)porphyrin iron(III) chloride, *Phys. Chem. Chem. Phys.*, 2018, **20**, 16985–16991.

17 P. Li, X. Zhang, C. Hou, Y. Chen and T. He, Highly efficient visible-light driven solar-fuel production over tetra(4-carboxyphenyl)porphyrin iron(III) chloride using CdS/Bi_2S_3 heterostructure as photosensitizer, *Appl. Catal., B*, 2018, **238**, 656–663.

18 A. Perazio, G. Lowe, R. Gobetto, J. Bonin and M. Robert, Light-driven catalytic conversion of CO_2 with heterogenized molecular catalysts based on fourth period transition metals, *Coord. Chem. Rev.*, 2021, **443**, 214018.

19 F. Arcudi, L. Đorđević, B. Nagasing, S. I. Stupp and E. A. Weiss, Quantum dot-sensitized photoreduction of CO_2 in water with turnover number >80,000, *J. Am. Chem. Soc.*, 2021, **143**, 18131–18138.

20 J. Wang, L. Jiang, H. Huang, Z. Han and G. Ouyang, Rapid electron transfer via dynamic coordinative interaction boosts quantum efficiency for photocatalytic CO_2 reduction, *Nat. Commun.*, 2021, **12**, 4276.

21 J. Bian, J. Feng, Z. Zhang, Z. Li, Y. Zhang, Y. Liu, S. Ali, Y. Qu, L. Bai, J. Xie, D. Tang, X. Li, F. Bai, J. Tang and L. Jing, Dimension-matched zinc phthalocyanine/$BiVO_4$ ultrathin nanocomposites for CO_2 reduction as efficient wide-visible-light-driven photocatalysts via a cascade charge transfer, *Angew. Chem., Int. Ed.*, 2019, **58**, 10873–10878.

22 J. Sun, J. Bian, J. Li, Z. Zhang, Z. Li, Y. Qu, L. Bai, Z. Yang and L. Jing, Efficiently photocatalytic conversion of CO_2 on ultrathin metal phthalocyanine/g-C_3N_4 heterojunctions by promoting charge transfer and CO_2 activation, *Appl. Catal., B*, 2020, **277**, 119199.

23 S. Xu, X. Li, S. Li, H. Rao, J.-S. Qin, P. She, W.-C. Cheong and L. Jing, Recent advances of photocatalytic CO_2 reduction based on hybrid molecular catalyst/semiconductor photocatalysts: A review, *Small*, 2025, **21**, 2408075.

24 S. McGuigan, S. J. Tereniak, C. L. Donley, A. Smith, S. Jeon, F. Zhao, R. N. Sampaio, M. Pauly, L. Keller, L. Collins, G. N.

Parsons, T. Lian, E. A. Stach and P. A. Maggard, Discovery of a hybrid system for photocatalytic CO_2 reduction via attachment of a molecular cobalt-quaterpyridine complex to a crystalline carbon nitride, *ACS Appl. Energy Mater.*, 2023, **6**, 10542–10555.

25 Y.-H. Li, Y. Chen, J.-Y. Guo, R. Wang, S.-N. Zhao, G. Li and S.-Q. Zang, Engineering coordination microenvironments of polypyridine Ni catalysts embedded in covalent organic frameworks for efficient CO_2 photoreduction, *Chin. J. Catal.*, 2025, **74**, 155–166.

26 J.-W. Wang, F. Zhao, H.-H. Huang, Z. Han and G. Ouyang, Molecular catalyst coordinatively bonded to organic semiconductors for selective light-driven CO_2 reduction in water, *Nat. Commun.*, 2024, **15**, 9779.

27 M. Schulz, M. Karnahl, M. Schwalbe and J. Vos, The role of the bridging ligand in photocatalytic supramolecular assemblies for the reduction of protons and carbon dioxide, *Coord. Chem. Rev.*, 2012, **256**, 1682–1705.

28 X. Wang, K. Maeda, A. Thomas, K. Takanabe, G. Xin, J. M. Carlsson, K. Domen and M. Antonietti, A metal-free polymeric photocatalyst for hydrogen production from water under visible light, *Nat. Mater.*, 2009, **8**, 76–80.

29 W. Ong, L. Tan, Y. Ng, S. Yong and S. Chai, Graphitic carbon nitride (g-C_3N_4)-based photocatalysts for artificial photosynthesis and environmental remediation: Are we a step closer to achieving sustainability?, *Chem. Rev.*, 2016, **116**, 7159–7329.

30 J. Wen, J. Xie, X. Chen and X. Li, A review on g-C_3N_4-based photocatalysts, *Appl. Surf. Sci.*, 2017, **391**, 72–123.

31 R. Umapathi, C. V. Raju, S. M. Ghoreishian, G. M. Rani, K. Kumar, M.-H. Oh, J. P. Park and Y. S. Huh, Recent advances in the use of graphitic carbon nitride-based composites for the electrochemical detection of hazardous contaminants, *Coord. Chem. Rev.*, 2022, **470**, 214708.

32 S. M. Ghoreishian, K. S. Ranjith, M. Ghasemi, B. Park, S.-K. Hwang, N. Irannejad, M. Norouzi, S. Y. Park, R. Behjatmanesh-Ardakani, S. M. Pourmortazavi, S. Mirsadeghi, Y.-K. Hanb and Y. S. Huh, Engineering the photocatalytic performance of B-C_3N_4@Bi_2S_3 hybrid heterostructures for full-spectrum-driven Cr(VI) reduction and in-situ H_2O_2 generation: Experimental and DFT studies, *Chem. Eng. J.*, 2023, **452**, 139435.

33 Y. Li, T. Kong and S. Shen, Artificial photosynthesis with polymeric carbon nitride: When meeting metal nanoparticles, single atoms, and molecular complexes, *Small*, 2019, **15**, 1900772.

34 Q. Chen, S. Li, H. Xu, G. Wang, Y. Qu, P. Zhu and D. Wang, Co-MOF as an electron donor for promoting visible-light photoactivities of g-C_3N_4 nanosheets for CO_2 reduction, *Chin. J. Catal.*, 2020, **41**, 514–523.

35 Q. Chen, G. Gao, Y. Zhang, Y. Li, H. Zhu, P. Zhu, Y. Qu, G. Wang and W. Qin, Dual functions of CO_2 molecular activation and 4f levels as electron transport bridges in erbium single atom composite photocatalysts therefore enhancing visible-light photoactivities, *J. Mater. Chem. A*, 2021, **9**, 15820–15826.

36 C. Li, H. Wu, D. Zhu, T. Zhou, M. Yan, G. Chen, J. Sun, G. Dai, F. Ge and H. Dong, High-efficient charge separation driven directionally by pyridine rings grafted on carbon nitride edge for boosting photocatalytic hydrogen evolution, *Appl. Catal., B*, 2021, **297**, 120433.

37 Z. Ma, X. Zong, Q. Hong, L. Niu, T. Yang, W. Jiang, D. Qu, L. An, X. Wang, Z. Kang and Z. Sun, Electrostatic potential of the incorporated asymmetry molecules induced high charge separation efficiency of the modified carbon nitride copolymers, *Appl. Catal., B*, 2022, **319**, 121922.

38 Q. Zhang, J. Chen, H. Che, P. Wang, B. Liu and Y. Ao, Recent advances in g-C_3N_4-based donor–acceptor photocatalysts for photocatalytic hydrogen evolution: An exquisite molecular structure engineering, *ACS Mater. Lett.*, 2022, **4**, 2166–2186.

39 Y. Wu, Z. Jiang, X. Lu, Y. Liang and H. Wang, Domino electroreduction of CO_2 to methanol on a molecular catalyst, *Nature*, 2019, **575**, 639–642.

40 S. Ren, D. Joulié, D. Salvatore, K. Torbensen, M. Wang, M. Robert and C. Berlinguette, Molecular electrocatalysts can mediate fast, selective CO_2 reduction in a flow cell, *Science*, 2019, **365**, 367–369.

41 W. W. Kramer and C. C. L. McCrory, Polymer coordination promotes selective CO_2 reduction by cobalt phthalocyanine, *Chem. Sci.*, 2016, **7**, 2506–2515.

42 K. E. R. Cruz, Y. Liu, T. L. Soucy, P. M. Zimmerman and C. C. L. McCrory, Increasing the CO_2 reduction activity of cobalt phthalocyanine by modulating the σ-donor strength of axially coordinating ligands, *ACS Catal.*, 2021, **11**, 13203–13216.

43 T. L. Soucy, W. S. Dean, J. Zhou, K. E. R. Cruz and C. C. L. McCrory, Considering the influence of polymer–catalyst interactions on the chemical microenvironment of electrocatalysts for the CO_2 reduction reaction, *Acc. Chem. Res.*, 2022, **55**, 252–261.

44 H. Niu, Y. Liu, B. Mao, N. Xin, H. Jia and W. Shi, In-situ embedding MOFs-derived copper sulfide polyhedrons in carbon nanotube networks for hybrid supercapacitor with superior energy density, *Electrochim. Acta*, 2020, **329**, 135130.

45 Z. Lin and X. Wang, Nanostructure engineering and doping of conjugated carbon nitride semiconductors for hydrogen photosynthesis, *Angew. Chem., Int. Ed.*, 2013, **52**, 1735–1738.

46 S. Morrison, *Electrochemistry at semiconductor and cxidized metal electrodes*, Plenum Press, New York, 1980.

47 A. Ishikawa, T. Takata, J. Kondo, M. Hara, H. Kobayashi and K. Domen, Oxysulfide $Sm_2Ti_2S_2O_5$ as a stable photocatalyst for water oxidation and reduction under visible light irradiation ($\lambda \leq 650$ nm), *J. Am. Chem. Soc.*, 2002, **124**, 13547–13553.

48 Y. Matsumoto, Energy positions of oxide semiconductors and photocatalysis with iron complex oxides, *J. Solid State Chem.*, 1996, **126**, 227–234.

49 Y. Matsumoto, K. Omae, I. Watanabe and E. Sato, Photoelectrochemical properties of the Zn-Ti-Fe spinel oxides, *J. Electrochem. Soc.*, 1986, **133**, 711–715.

50 S. Roy and E. Reisner, Visible-light-driven CO_2 reduction by mesoporous carbon nitride modified with polymeric cobalt phthalocyanine, *Angew. Chem., Int. Ed.*, 2019, **58**, 12180–12184.

51 S. M. Ghoreishian, K. S. Ranjith, H. Lee, H. Ju, S. Z. Nikoo, Y.-K. Han and Y. S. Huh, Hierarchical N-doped

TiO_2@$Bi_2W_xMo_{1-x}O_6$ core-shell nanofibers for boosting visible–light–driven photocatalytic and photoelectrochemical activities, *J. Hazard. Mater.*, 2020, **391**, 122249.

52 S. M. Ghoreishian, K. S. Ranjith, B. Park, S.-K. Hwang, R. Hosseini, R. Behjatmanesh-Ardakani, S. M. Pourmortazavi, H. U. Lee, B. Son, S. Mirsadeghi, Y.-K. Han and Y. S. Huh, Full-spectrum-responsive Bi_2S_3@CdS S-scheme heterostructure with intimated ultrathin RGO toward photocatalytic Cr(VI) reduction and H_2O_2 production: Experimental and DFT studies, *Chem. Eng. J.*, 2021, **419**, 129530.

53 F. Moser and A. Thomas, *The Phthalocyanines, Vol. II: Properties*, CRC Press, Boca Raton, 1983.

54 M. Frisch, *et al.*, *Gaussian 09, Revision D.01*, Gaussian, Inc., Wallingford CT, 2016.